Preliminary study on estimation of flow velocity vectors using focused transmit beams

Japanese Journal of Applied Physics **61**, SG1026 (2022) **REGULAR PAPER**
https://doi.org/10.35848/1347-4065/ac4687

Preliminary study on estimation of flow velocity vectors using focused transmit beams

Hideyuki Hasegawa[1*], Michiya Mozumi[2], Masaaki Omura[1], Ryo Nagaoka[1], and Kozue Saito[3]

[1]*Faculty of Engineering, University of Toyama, Toyama 930-8555, Japan*
[2]*Graduate School of Science and Engineering for Education, University of Toyama, Toyama 930-8555, Japan*
[3]*Department of Neurology, Nara Medical University, Nara 634-8521, Japan*

[*]E-mail: hasegawa@eng.u-toyama.ac.jp

Received October 28, 2021; revised December 22, 2021; accepted December 26, 2021; published online March 23, 2022

High-frame-rate ultrasound imaging with plane wave transmissions is a predominant method of blood flow imaging, and methods for estimation of blood flow velocity vectors have been developed based on high-frame-rate imaging. On the other hand, in imaging of soft tissues, such as arterial walls and atherosclerotic plaques, high-frame-rate imaging sometimes suffers from high-level clutters. Even in observation of the arterial wall with a focused transmit beam, it would be highly beneficial if blood flow velocity vectors could be estimated simultaneously. We conducted a preliminary study on the estimation of blood flow velocity vectors based on a multi-angle Doppler method with focused transmit beam and parallel receive beamforming. It was shown that the lowest estimation error was achieved at a steering angle of 25° by simulation. Moreover, velocity vectors with typical velocity magnitudes and directions could be obtained by the proposed method in in vivo measurement of a carotid artery.

1. Introduction

Owing to the predominant temporal resolution of diagnostic ultrasound imaging, it is preferable for the measurement of tissue dynamical properties, such as blood flow. High-frame-rate ultrasound imaging with unfocused transmit beams, e.g. a plane wave and a spherically diverging wave, further strengthens such a characteristic of ultrasound imaging.[1–6] High-frame-rate ultrasound imaging achieves an extremely high temporal resolution of several thousand frames per second. However, resolution and contrast are degraded compared with line-by-line imaging with a focused transmit beam. Spatial compound imaging[7] was developed to solve such an issue by coherently compounding beamformed radio-frequency (RF) signals obtained from multiple transmissions of plane waves at different steering angles. High-frame-rate ultrasound imaging was shown to be of great value in the measurement of a rapidly propagating shear wave, which is induced by ultrasonic acoustic radiation force,[6] and also applied to the measurement of vascular dynamics, such as arterial wall motion and blood flow.[8–13] The ultrafast compound Doppler method[13] achieves better contrast than conventional color flow imaging and was shown to be feasible in imaging of small flows in the myocardium[14] and brain.[15,16] On the other hand, the ultrafast compound Doppler method is still limited to measurement of only the axial flow velocity. To overcome such a problem, angle-independent velocity estimators, such as 2D correlation[17–19] and the multi-angle Doppler method,[20–22] were introduced in blood flow imaging. Although the ultrafast compound Doppler method and multi-angle Doppler method realize high-contrast and angle-independent blood flow imaging, respectively, the aliasing limit (maximum detectable velocity) is lowered by increasing the number of transmissions (plane waves at different steering angles). To overcome such a limitation, the repeated transmit sequence was developed and introduced in the ultrafast compound Doppler method,[23] in which plane waves were transmitted in the same direction twice before changing the steering angle. By applying the autocorrelation method[24] to the beamformed signals obtained from the two consecutive emissions in the same direction, the aliasing limit could be kept as that determined by the pulse repetition frequency (PRF). We realized a multi-angle Doppler method with plane wave imaging and repeated transmit sequence to obtain blood flow velocity vectors without reducing the aliasing limit.[25,26]

As described above, high-frame-rate ultrasound imaging is promising for detailed analyses of blood flow dynamics. On the other hand, high-frame-rate ultrasound imaging produces higher-level clutters than conventional imaging with focused beams. Moreover, recently harmonic imaging has been used in most cases of measurement of soft tissues like arterial walls to reduce clutters further. However, it is difficult to realize tissue harmonic imaging in high-frame-rate imaging because unfocused transmit beams cannot produce sufficiently high sound pressure for generation of harmonic components. A low sound pressure level of an unfocused beam also presents difficulty in observation of a difficult-to-image subject in which ultrasound is attenuated significantly due to a deep location of a vessel. To overcome such limitations, we showed the possibility of measurement of blood flow velocity vectors with focused transmit beams at a higher temporal resolution than conventional line-by-line imaging.[27] In the present study, an appropriate transmit–receive condition for such a blood flow measurement with focused transmit beams was investigated in detail by numerical simulation. For in vivo measurements, a clutter filter was designed specifically for the investigated transmit–receive sequence. Finally, the feasibility of the proposed method was demonstrated by an in vivo measurement of blood flow velocity vectors in a human carotid artery.

2. Materials and methods

2.1. Multi-line transmission and reception

In the present study, the imaging frame rate was increased using parallel beamforming both in transmission and reception. In transmission, two non-steered beams focused at a depth of 20 mm were generated in parallel, as illustrated by the arrows with solid lines in Fig. 1(a). The distance between the centers of the two transmit apertures was $\beta \cdot \delta x$, where β

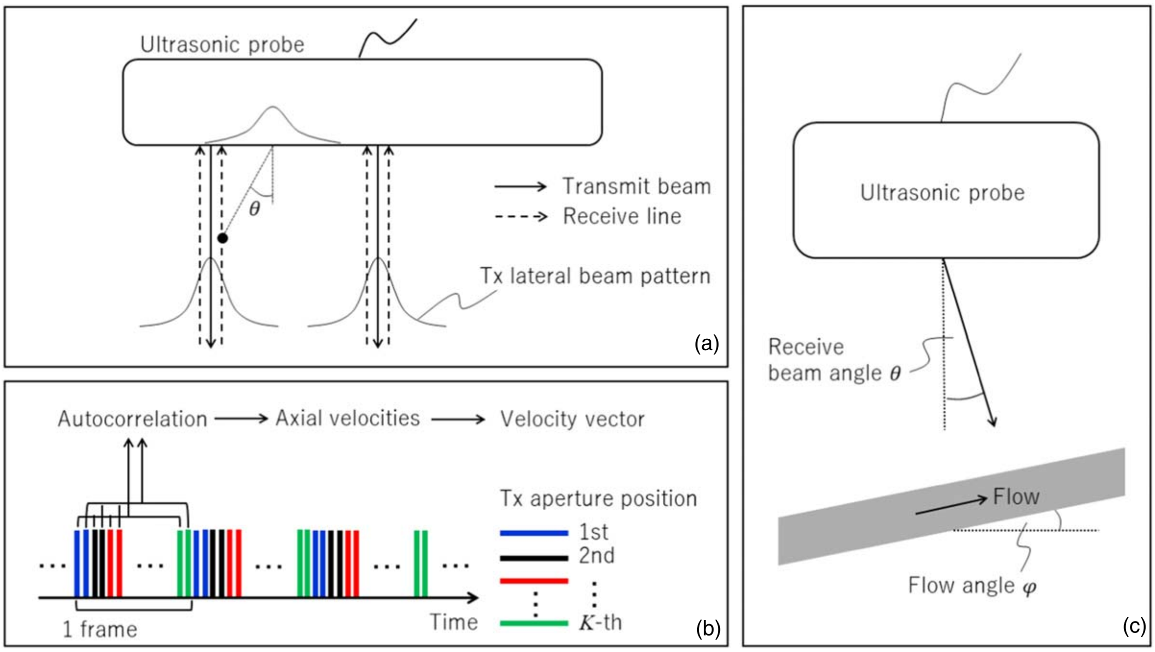

Fig. 1. (Color online) Illustrations of transmit (Tx)–receive (Rx) sequences. (a) Multi-line transmission and reception. (b) Transmission (Tx) sequence. (c) Geometry in numerical simulation.

is a coefficient (set at 60 in the present study) determining the lateral spacing between the two parallel transmit beams and δx (=0.2 mm) is the element pitch. A Tukey function at a coefficient of 0.4 was used as transmit apodization by referring to our previous study.[26)]

In reception, beamformed RF signals were created based on delay-and-sum (DAS) beamforming by setting receiving focal points along the two parallel receive lines (illustrated by the arrows with dashed lines in Fig. 1) at vertical intervals of $\delta z = 0.025$ mm. The sound pressures of the transmit beams along these parallel receive beams are the same when the transmit beams are laterally symmetrical. The distance between the centers of the transmit beam and each receive line was set at half the element pitch (=0.1 mm), resulting in lateral spacing of receive lines of 0.2 mm. By denoting the lateral and vertical positions of a focal point as x and z, respectively, the forward propagation distance from the transmit aperture to the focal point was considered as $r_{\mathrm{tx}} = z$ by assuming that the transmitted wave is locally a plane wave.

In reception, beamformed RF signals were created at receiving steering angles of θ_l $(l = 0, 1, 2, \ldots, L-1)$ at every focal point to estimate velocity vectors, where L is the number of receiving steering angles. As illustrated in Fig. 1, the lateral position of the receiving aperture x_{r} was determined using receive apodization, i.e. a Gaussian function, the position of which was dependent on the receive steering angle. The lateral position of the center of the receiving aperture x_{r} is expressed as

$$x_{\mathrm{r}} = x - z \tan \theta_l. \tag{1}$$

The F-number in receive beamforming was set at 2.08, where the size of the receiving aperture was defined by the full width at half maximum of the Gaussian function. The backward propagation distance r_{rx} from the focal point to the ith element is expressed as

$$r_{\mathrm{rx}} = \{(x - x_i)^2 + z^2\}^{\frac{1}{2}}, \tag{2}$$

where x_i is the lateral position of the ith element.

Based on such a procedure, four receive lines were produced at each receiving steering angle θ_l by a single transmit–receive event [(2 transmit beams) × (2 receive lines)]. In the present study, $M_x = 120$ receive lines at pitches of 0.2 mm were produced at each receiving steering angle θ_l by changing the transmit position by $M_{\mathrm{p}} = 30$ times and repeating the same procedure, where the translation pitch of the transmit apertures was 0.4 mm (two elements).

The temporal transmit–receive sequence used in the present study is illustrated in Fig. 1(b). For the subsequent Doppler processing, the transmit–receive procedure was repeated twice before changing the positions of the transmit apertures. As is widely known, Doppler processing suffers from the aliasing effect, and the time interval between received signals should be as short as possible to increase the maximum detectable velocity. By correlating echoes obtained by these two consecutive transmit–receive events at the same transmit position, the time interval becomes the shortest, which corresponds to the pulse repetition interval (PRI) T_{PRI}.

2.2. Estimation of velocity vectors

A measurement of flow velocity under the geometry shown in Fig. 1(c) is considered in the present study. Let us define the complex analytic signal of the beamformed signal obtained by the procedure described in the previous section as $s(m_x, m_z, n, k, \theta_l)$, where m_x, m_z, n, and k are the lateral sampling number $(m_x = 0, 1, 2, \ldots, M_x - 1; M_x = 120)$, vertical sampling number $(m_z = 0, 1, 2, \ldots, M_z - 1; M_z = 1200)$, frame number $(n = 0, 1, 2, \ldots, N - 1; N = 200)$, and transmission number at each transmit aperture position $(k = 1, 2)$, respectively. The complex correlation function $\gamma(m_x, m_z, n; \delta m_z, \delta k)$ is expressed as

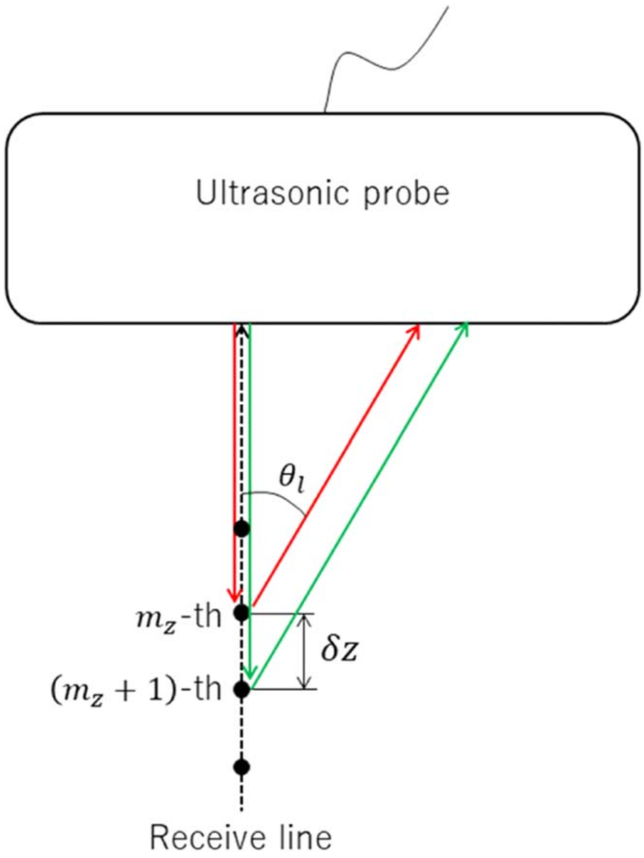

Fig. 2. (Color online) Illustration of transmit–receive propagation distance.

$$\gamma(m_x, m_z, n; \delta m_z, \delta k) = \sum_R s^*(m_x, m_z, n, k, \theta_l) \cdot s(m_x, m_z + \delta m_z, n, k + \delta k, \theta_l), \tag{3}$$

where δm_z and δk are spatial (vertical) and temporal lags, respectively, and R denotes a two-dimensional kernel. The lateral and vertical kernel sizes were empirically set at 1.4 mm and 0.925 mm, respectively, by referring to the previous study.[26]

The axial velocity $v_{ax}(m_x, m_z, n; \theta_l)$ is obtained as follows[24]:

$$v_{ax}(m_x, m_z, n; \theta_l) = \frac{c_0}{4\pi f_0 T_{PRI}} \angle \gamma(m_x, m_z, n; 0, 1), \tag{4}$$

where c_0, f_0, and $\angle$ denote the speed of sound, ultrasonic center frequency, and phase angle of a complex value, respectively. As reported previously, the center frequency f_0 of the received ultrasonic signal varies due to interference among echoes from scatterers.[26,28] Therefore, in the present study, the center frequency f_0 was also estimated from the received ultrasonic echoes. The propagation path of an ultrasonic signal received at receiving steering angle θ_l is considered as illustrated in Fig. 2. Let us express the echo signal from the m_zth sampled point as a sinusoidal wave at center frequency f_0:

$$s(m_x, m_z, n, k, \theta_l) = e^{j2\pi f_0 t}, \tag{5}$$

where the variation in the echo amplitude is omitted.

Let us consider the change in the signal phase depending on the propagation path length. In estimation of the axial velocity at (m_x, m_z), the differences in ultrasonic propagation path lengths were calculated between the m_zth and $(m_z + 1)$th sampled points and between the $(m_z - 1)$th and m_zth sampled points. The difference d_1 between the propagation path lengths of the echo signals from the m_zth and $(m_z + 1)$th sampled points is expressed as

$$d_1 = \delta z + [\{(m_z + 1)\delta z\}^2 + \{(m_z + 1)\delta z \cdot \tan\theta_l\}^2]^{\frac{1}{2}} - \{(m_z \cdot \delta z)^2 + (m_z \cdot \delta z \cdot \tan\theta_l)^2\}^{\frac{1}{2}}. \tag{6}$$

Similarly, the difference d_2 between the propagation path lengths of the echo signals from the $(m_z - 1)$th and m_zth sampled points is expressed as

$$d_2 = \delta z + \{(m_z \cdot \delta z)^2 + (m_z \cdot \delta z \cdot \tan\theta_l)^2\}^{\frac{1}{2}} - [\{(m_z - 1)\delta z\}^2 + \{(m_z - 1)\delta z \cdot \tan\theta_l\}^2]^{\frac{1}{2}}. \tag{7}$$

Such calculations of the propagation path lengths are the same as that in synthetic aperture imaging.[29] Based on the model expressed by Eq. (5), the relationships expressed by Eqs. (8) and (9) are obtained as:

$$\gamma(m_x, m_z, n; 1, 0) = \mathrm{E}_R[s^*(m_x, m_z, n, 0, \theta_l) \cdot s(m_x, m_z +, n, 0, \theta_l)] = e^{j\frac{2\pi f_0 d_1}{c_0}}. \tag{8}$$

$$\gamma(m_x, m_z, n; -1, 0) = \mathrm{E}_R[s^*(m_x, m_z, n, 0, \theta_l) \cdot s(m_x, m_z - 1, n, 0, \theta_l)] = e^{-j\frac{2\pi f_0 d_2}{c_0}}. \tag{9}$$

From Eqs. (7) and (8), the center frequency f_0 is estimated as follows:

$$\hat{f}_0 = \frac{c_0}{2\pi(d_1 + d_2)} \angle\{\gamma^*(m_x, m_z, n; -1, 0) \cdot \gamma(m_x, m_z, n; 1, 0)\}. \tag{10}$$

Lateral and vertical velocities $v_x(m_x, m_z, n)$ and $v_z(m_x, m_z, n)$ are expressed using the axial velocities $v_{ax}(m_x, m_z, n; \theta_l)$ obtained at different receiving steering angles θ_l as[20–22]

$$v_x(m_x, m_z, n)\sin\theta_l + v_z(m_x, m_z, n)(1 + \cos\theta_l) = 2v_{ax}(m_x, m_z, n; \theta_l). \tag{11}$$

The relationship expressed by Eq. (11) can be summarized as

$$\begin{bmatrix} \sin\theta_0 & 1 + \cos\theta_0 \\ \vdots & \vdots \\ \sin\theta_{L-1} & 1 + \cos\theta_{L-1} \end{bmatrix} \begin{bmatrix} v_x(m_x, m_z, n) \\ v_z(m_x, m_z, n) \end{bmatrix} = \begin{bmatrix} 2v_{ax}(m_x, m_z, n; \theta_0) \\ \vdots \\ 2v_{ax}(m_x, m_z, n; \theta_{L-1}) \end{bmatrix}$$

$$\Rightarrow \mathbf{A}\mathbf{v} = \mathbf{v}_{ax}. \tag{12}$$

The velocity vector $\mathbf{v}$ is estimated by the least-squares method as

$$\hat{\mathbf{v}} = (\mathbf{A}^T\mathbf{A})^{-1}\mathbf{A}^T\mathbf{v}_{ax}, \tag{13}$$

where ^{T} denotes the transpose, and $(\mathbf{A}^T\mathbf{A})^{-1}\mathbf{A}^T$ is the pseudoinverse of $\mathbf{A}$.

2.3. Clutter filter for in vivo experiment

As part of in vivo measurements of arteries, a clutter filter is required to suppress strong echoes from slowly moving tissues and enhance weak echoes from rapidly moving blood cells. In conventional color flow imaging, transmit–receive events are repeated several times (typically 8–16) at each scan line to apply a clutter filter to the received signal in the scan line. Therefore, a number of transmissions are required to acquire a set of data for one frame. In the present study, the number of transmissions per line was set at 2 to reduce the number of transmissions per frame. On the other hand, a traditional clutter filter cannot be applied to the received signals in each line.

In the present study, singular value decomposition (SVD) was used as a clutter filter[30,31] and applied to beamformed complex RF signals in a way inspired by our previous study.[25] SVD was separately applied to two groups of signals $s(m_x, m_z, n, 0, \theta_l)$ and $s(m_x, m_z, n, 1, \theta_l)$ ($n = 0, 1, 2, \ldots, N$), i.e. the datasets obtained by the first and second emissions in each receive line. Each dataset was composed of ($M_x \times M_z \times N$) samples. A 2D Casorati matrix $\mathbf{S}$ of dimensions ($M_x M_z \times N$) was obtained from each dataset. This matrix can be decomposed as

$$\mathbf{S} = \mathbf{U}\boldsymbol{\Sigma}\mathbf{V}^{\mathrm{T}}, \tag{14}$$

where $\mathbf{U}$ and $\mathbf{V}$ are matrices composed of spatial and temporal singular vectors, respectively, and $\boldsymbol{\Sigma}$ is a diagonal matrix composed of singular values arranged in descending order. The SVD filtered signal matrix $\hat{\mathbf{S}}$ is obtained as

$$\hat{\mathbf{S}} = \mathbf{U}\boldsymbol{\Sigma}_{\mathrm{t}}\mathbf{V}^{\mathrm{T}}, \tag{15}$$

where $\boldsymbol{\Sigma}_{\mathrm{t}}$ is obtained from $\boldsymbol{\Sigma}$ by replacing the high- and low-order singular values with zeros. In the present study, low and high thresholds to the singular values were assigned empirically. The filtered signals were rearranged in the order of the signals before filtering and processed by the principle described in Sect. 2.2.

2.4. Method of simulation

The accuracy in estimation of velocity vectors by the proposed method was validated by numerical simulation. The simulated transmit–receive sequence was the same as that described in Sect. 2.1. In receive beamforming, the receiving steering angles θ_l were set at $-\theta_{\max}$, 0, and $\theta_{\max}$ ($L = 3$). The effects of the maximum steering angle $\theta_{\max}$ were evaluated by changing $\theta_{\max}$ from 5° to 40° at intervals of 5°.

A simulated flow phantom was created by distributing point scatterers randomly in the form of a cylinder. The radius of the cylinder was set at $r_0 = 2.5$ mm. Since typical tilt angles of carotid arteries are less than 10°, tilt angles of 0° and 10° were examined in the present study. A parabolic flow profile was simulated by moving the distributed scatterers parallel to the central axis of the cylinder. The moving velocity $v(r)$ at the radial position r is expressed as

$$v(r) = v_{\max}\frac{(r_0 - r)^2}{r_0^2}, \tag{16}$$

where $v_{\max}$ is the maximum velocity at the central axis of the cylinder. The accuracy in velocity estimation was evaluated under different maximum velocities $v_{\max}$ from 0.1, 0.2, 0.4, and 0.8 m s^{-1}.

In the numerical simulation, echo signals obtained by the transmit-receive sequence described in Sect. 2.1 were generated with the Field II simulation software.[32,33] A 7.5 MHz linear array probe with the same specifications as the real probe used in the in vivo measurement was simulated. The PRI was set at 100 μs.

2.5. Evaluation of errors in estimated velocity

Since the true velocities are known in the numerical simulation, the errors in the estimated velocities were evaluated.[26] The absolute bias error (ABE) was evaluated as

$$ABE = |\mathrm{E}_{R_{\mathrm{f}}}[\mathbf{v}_{\mathrm{est}} - \mathbf{v}_{\mathrm{tru}}]|, \tag{17}$$

where $\mathbf{v}_{\mathrm{est}}$ and $\mathbf{v}_{\mathrm{tru}}$ are estimated and true velocity vectors, respectively, and $E_{R_{\mathrm{f}}}[\,\cdot\,]$ denotes the expectation with respect to the flow region R_{f}. To evaluate errors which were fluctuating spatially, the root mean squared error excluding bias error (RMSEexBE) was evaluated by assuming that the component of the bias error and the spatially fluctuating component are independent. RMSEexBE is defined as

$$\mathrm{RMSEexBE} = \sqrt{E_{R_{\mathrm{f}}}[|\mathbf{v}_{\mathrm{est}} - \mathbf{v}_{\mathrm{tru}}|^2] - \mathrm{ABE}^2}. \tag{18}$$

Both errors described above were calculated as the relative value with respect to the assigned maximum velocity $v_{\max}$.

2.6. Acquisition system

In the in vivo measurement of a human carotid artery, a 7.5 MHz linear array probe with 192 transducer elements at pitches of 0.2 mm (UST-5412, Fujifilm) was used. The linear array probe was connected to a custom-made acquisition system (RSYS0016, Microsonic) with 256 transmit–receive channels. The transmit–receive events were performed as described in Sect. 2.1 at a PRI of 96 μs. The received echo signals were sampled at 31.25 MHz for off-line processing using custom-made software based on MATLAB (MathWorks). In receive beamforming, the receiving steering angles θ_l were set at $-\theta_{\max}$, 0, and $\theta_{\max}$ ($L = 3$). The maximum steering angle $\theta_{\max}$ was set at the value determined by the numerical simulation.

3. Results

Figure 3 shows an example of the results on the numerical simulation. Figure 3(a) shows a B-mode image of the simulation phantom obtained at flow tilt angle φ and maximum flow velocity $v_{\max}$ of 10° and 0.1 m s^{-1}, respectively. Figures 3(b) and 3(c) are lateral and vertical velocities estimated by the proposed method with a maximum receiving steering angle $\theta_{\max}$ of 25°. In this case, ABE and RMSEexABE were 1.1% and 13.8%, respectively. ABE and RMSEexABE were also evaluated under different flow tilt angles φ and maximum receiving steering angles $\theta_{\max}$ and summarized in Fig. 4. In Fig. 4, the effects of estimation of the center frequency f_0 of the received signals are also examined. The plots and vertical bars in Fig. 4 correspond to ABEs and RMSEexABEs evaluated by Eqs. (17) and (18), respectively. ABEs and RMSEexABEs show the bias and spatial variation in the estimated velocity vectors, respectively. As shown in Fig. 4, the accuracy in estimation of flow velocity vectors is improved significantly by estimating the center frequency f_0 independently of the flow tilt angle φ. Moreover, the accuracy in estimation of flow velocity vectors was best when the maximum receiving steering angle $\theta_{\max}$ was 25°, while RMSEexABEs did not vary significantly at maximum receiving steering angles $\theta_{\max}$ of over 20°.

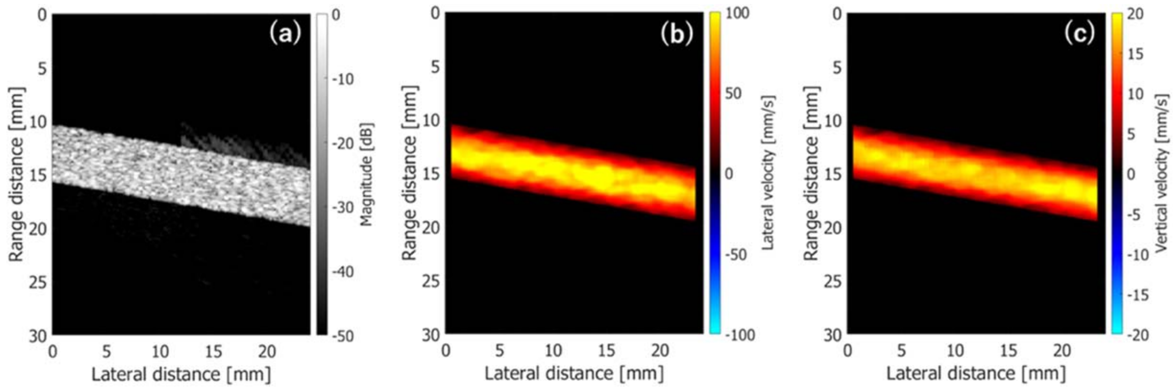

Fig. 3. (Color online) Results of simulation. (a) B-mode image of simulation phantom. (b) Estimated lateral velocity. (c) Estimated vertical velocity.

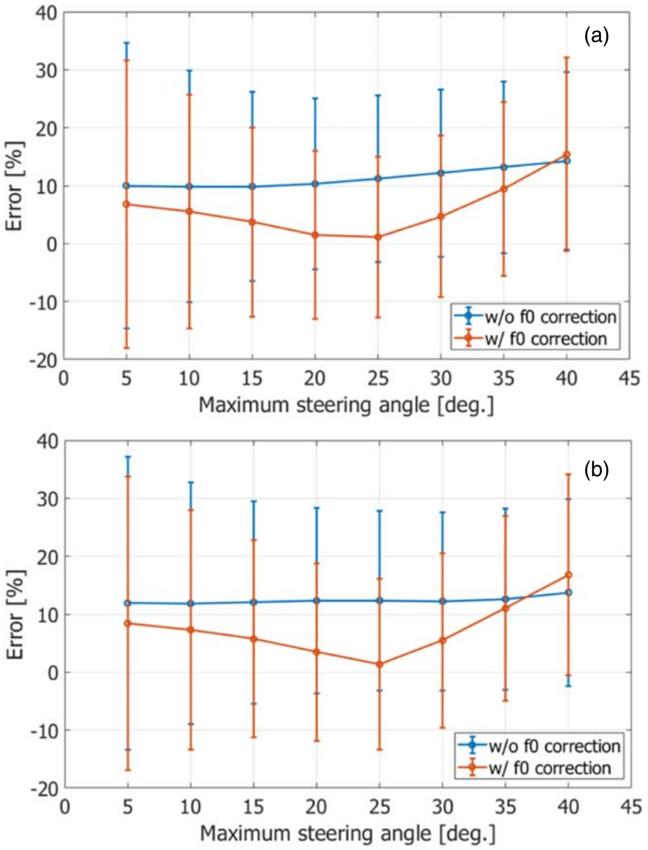

Fig. 4. (Color online) Errors in estimated velocities obtained without and with center frequency estimation. (a) Flow tilt angle of 0°. (b) Flow tilt angle of 10°.

Therefore, the maximum receiving steering angle θ_{max} was set at 25° in the subsequent in vivo measurement. Furthermore, as shown in Fig. 5, the proposed method can estimate the flow velocity vectors with consistent ABEs and RMSEexABEs under the investigated maximum flow velocity v_{max}, independently of the investigated flow tilt angle φ.

Figure 6(a) shows a B-mode image of a human carotid artery of a 47-year-old healthy male. To enhance weak echoes from blood cells, the SVD clutter filter described in Sect. 2.3 was applied to the beamformed complex RF signal obtained at each receiving steering angle θ_l, and a B-mode image constructed from the filtered signal is shown in Fig. 6(b). The maximum receiving steering angle θ_{max} was set at 25°. As can be seen in Fig. 6(b), echoes from blood cells were enhanced successfully.

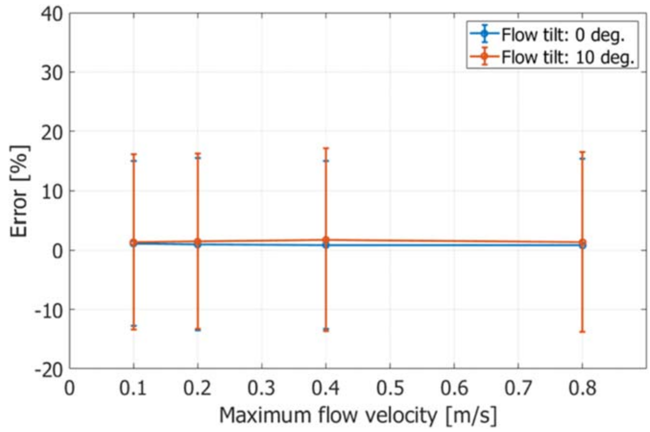

Fig. 5. (Color online) Errors in estimated velocities obtained at flow tilt angles of 0° and 10° plotted as functions of true maximum flow velocity.

Figure 7 shows the profiles of singular values obtained in SVD clutter filtering obtained at the respective receiving steering angles. The magnitude values in Fig. 7 were obtained by applying SVD to the received signals sampled at a resolution of 12 bits. As can be seen in Fig. 7, the transmit–receive sensitivities at maximum receiving steering angles of −25° and 25° were lower than that at 0°. Therefore, the thresholds to the singular values in SVD filtering were assigned differently depending on the receiving steering angle θ_l. The thresholds to the low- and high-order singular values were empirically set at 75 and 71 dB, respectively, for a receiving steering angle of 0° and 71 and 67 dB, respectively, for receiving steering angles of −25° and 25° by referring to the inflection points in the profiles of the singular values.

The proposed method for estimation of flow velocity vectors was applied to the SVD filtered signals, and the estimated flow velocity vectors are shown in Fig. 6(c). Figure 6(c) is a flow velocity distribution in cardiac systole, and the maximum flow velocity is around 0.4 m s^{-1}, which is in the physiological range of the flow velocity in a carotid artery. Also, the directions of the estimated flow velocity are consistent. This result shows that the proposed method is feasible in an in vivo measurement of flow velocity vectors.

4. Discussion

Blood flow imaging is an important function in medical diagnostic ultrasound. Although color flow imaging is widely used in ultrasonic measurement of blood flow, only velocity

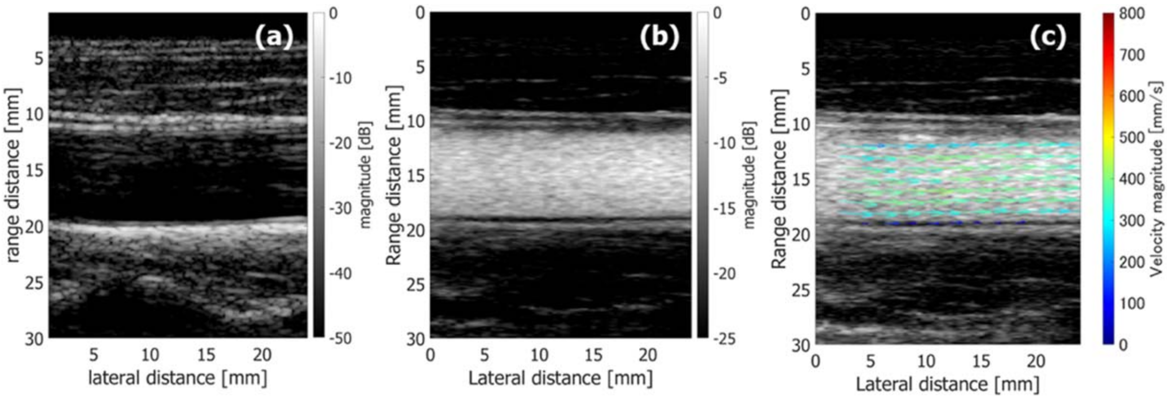

Fig. 6. (Color online) In vivo experimental results on a 47-year-old male. (a) B-mode image. (b) Clutter-filtered B-mode image. (c) Estimated velocity vectors overlaid on B-mode image reconstructed from clutter-filtered ultrasonic signals.

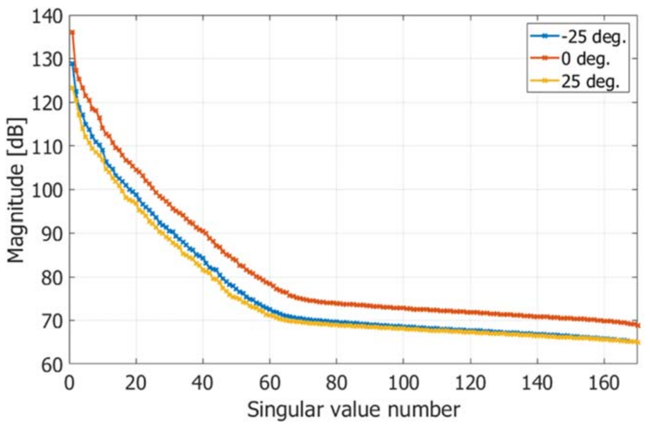

Fig. 7. (Color online) Distribution of singular values obtained from in vivo experimental data on carotid artery.

components in the axial direction are measured. High-frame-rate ultrasound imaging enables angle-independent measurement of flow velocity. However, high-frame-rate ultrasound imaging sometimes suffers from high-level clutters in imaging of soft tissues due to unfocused transmit beams. To realize estimation of flow velocity vectors, the vector flow mapping (VFM) method was developed and estimated flow velocity vectors from axial velocities obtained by color flow imaging with the theory of fluid dynamics.[34] However, with such a theoretical analysis it is difficult to estimate flow velocity vectors at a site with flow disturbance by atherosclerotic plaque. The proposed method enables estimation of flow velocity vectors with focused transmit beams without fluid dynamic assumptions.

In conventional color flow imaging, the transmit–receive event is required to be repeated several times for clutter filtering and keeping the maximum detectable velocity (aliasing limit) as high as possible. Therefore, a number of transmit–receive events, i.e. (number of repetitions per scan line) times (number of scan lines), are required to acquire a dataset for one frame. This results in significant reduction of the frame rate. With a specifically designed clutter filter, the proposed method could reduce the number of transmit–receive events to two. Consequently, only 60 transmit–receive events are required for one frame, which corresponds to a frame rate of 173.6 frames per second (fps) at a PRI of 96 μs.

In the validation by the numerical simulation, a receiving steering angle of 25° achieved the best performance. The receiving steering angle is considered to be limited due to a finite size of the physical aperture. Figure 8(a) illustrates the size of the imaging region and the center positions of the left and right most receiving apertures. As illustrated in Fig. 8(a), the distance between the center positions of the left- and rightmost receiving apertures is $(L + 2W)$. When the maximum imaging depth is 20 mm, $L + 2W = 38.6$ mm at $\theta_{max} = 20°$, which almost corresponds to a physical aperture size of 38.4 mm. Therefore, the estimation error increased gradually when the maximum receiving steering angle θ_{max} was larger than 25°. Figure 8(b) shows a vertical velocity distribution estimated at a maximum steering angle, maximum flow velocity, and flow tilt angle of 30°, 100 mm s^{-1}, and 0°, respectively. In this case, the estimated vertical flow velocities should be zero at all positions because the flow tilt angle is zero. However, large errors occur only in the regions around both edges of the field of view. This result suggests that one of the receiving beams is not formed appropriately at a large steering angle because of the limitation in the physical size of the ultrasonic probe. An ultrasonic probe with a larger physical aperture would increase the maximum imaging depth and might improve the estimation accuracy by completely forming receiving beams across the entire field of view. In our future work, we will fabricate such a probe for more accurate velocity estimation in a wider field of view.

In the present study, center frequencies of received signals were estimated using their phases. The center frequency would also be estimated by calculating their frequency spectra. However, such a method of estimation of the center frequency requires a Fourier transform at each position in the beamforming grid. The proposed method uses phases of received signals to reduce the computational cost. In estimation of the center frequency, the center frequency was estimated using the information on the ultrasonic propagation path lengths calculated by Eqs. (6) and (7). However, the path length estimation might be influenced by the beamforming condition. More accurate estimation of the propagation path length might improve the accuracy in estimation of the center frequency and velocity vector. Furthermore, the effect of the center frequency estimation was examined by evaluating the accuracy in estimation of velocity vectors. An investigation on the accuracy in estimation of center frequencies themselves would elucidate the underlying principle for further reduction of the influence of the center frequency variation.

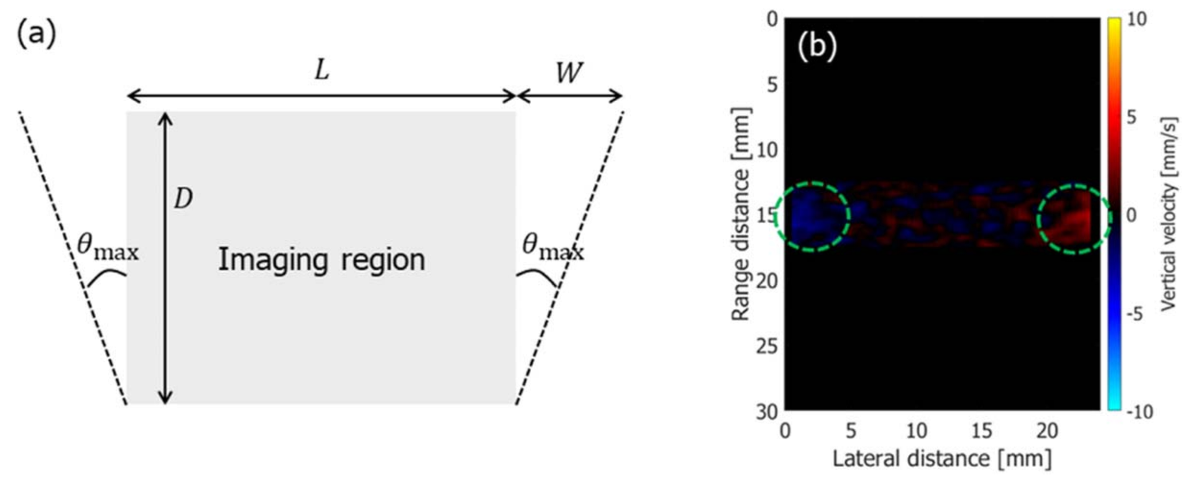

Fig. 8. (Color online) (a) Illustration of imaging field of view and steered receiving beams. (b) Vertical velocity distribution estimated at a maximum steering angle, maximum flow velocity, and flow tilt angle of 30°, 100 mm s^{-1}, and 0°, respectively.

5. Conclusions

This study presented a method for estimation of blood flow velocity vectors using parallel beamforming with focused transmit beams. Using packet transmit sequence, which repeated a transmit–receive sequence before translating the aperture position, the maximum detectable velocity could be kept as high as possible. Moreover, by limiting the number of repetitions of the transmit–receive event in each scan line to two, a frame rate of 173.6 fps, which is significantly higher than that in conventional color flow imaging, could be realized. Such a method for estimation of blood flow velocity vectors would be useful for detailed analyses of flow dynamics in vasculatures.

Acknowledgments

This study was supported by JSPS KAKENHI Grant Nos. 18KK0110 and 19K22891.

ORCID iDs

Hideyuki Hasegawa https://orcid.org/0000-0003-0709-7821
Masaaki Omura https://orcid.org/0000-0002-4432-8548
Ryo Nagaoka https://orcid.org/0000-0002-6713-8106
Kozue Saito https://orcid.org/0000-0002-0630-4342

1) C. Bruneel, R. Torguet, K. M. Rouvaen, E. Bridoux, and B. Nongaillard, Appl. Phys. Lett. **30**, 371 (1977).
2) B. Delannoy, R. Torguet, C. Bruneel, E. Bridoux, J. M. Rouaven, and H. Lasota, J. Appl. Phys. **50**, 3153 (1979).
3) D. Shattuck, M. Weinshenker, S. Smith, and O. von Ramm, J. Acoust. Soc. Am. **75**, 1273 (1984).
4) S. W. Smith, H. G. Pavy Jr, and O. T. von Ramm, IEEE Trans. Ultrason. Ferroelectr. Freq. Control **38**, 100 (1991).
5) O. T. von Ramm, S. W. Smith, and H. G. Pavy Jr, IEEE Trans. Ultrason. Ferroelectr. Freq. Control **38**, 109 (1991).
6) M. Tanter, J. Bercoff, L. Sandrin, and M. Fink, IEEE Trans. Ultrason. Ferroelectr. Freq. Control **49**, 1363 (2002).
7) G. Montaldo, M. Tanter, J. Bercoff, N. Benech, and M. Fink, IEEE Trans. Ultrason. Ferroelectr. Freq. Control **56**, 489 (2009).
8) H. Hasegawa and H. Kanai, 2008 IEEE Intern'l. Ultrason. Symp. Proc., p. 225, 2008.
9) H. Hasegawa and H. Kanai, IEEE Trans. Ultrason. Ferroelectr. Freq. Control **55**, 2626 (2008).
10) J. Vappou, J. W. Luo, and E. E. Konofagou, Am. J. Hypertens. **23**, 393 (2010).
11) M. Couade, M. Pernot, E. Messas, J. Emmerich, A. Hagege, M. Fink, and M. Tanter, IRBM **32**, 106 (2011).
12) J. Luo, R. X. Li, and E. E. Konofagou, IEEE Trans. Ultrason. Ferroelectr. Freq. Control **59**, 174 (2012).
13) J. Bercoff, G. Montaldo, T. Loupas, D. Savery, F. Meziere, M. Fink, and M. Tanter, IEEE Trans. Ultrason. Ferroelectr. Freq. Control **58**, 134 (2011).
14) B. F. Osmanski, M. Pernot, G. Montaldo, A. Bel, E. Messas, and M. Tanter, IEEE Trans. Med. Imaging **31**, 1661 (2012).
15) E. Mace, G. Montaldo, I. Cohen, M. Baulac, M. Fink, and M. Tanter, Nat. Methods **8**, 662 (2011).
16) E. Mace, G. Montaldo, B. F. Osmanski, I. Cohen, M. Fink, and M. Tanter, IEEE Trans. Ultrason. Ferroelectr. Freq. Control **60**, 492 (2013).
17) J. Udesen, F. Gran, K. L. Hansen, J. A. Jensen, C. Thomsen, and M. B. Nielsen, IEEE Trans. Ultrason. Ferroelectr. Freq. Control **55**, 1729 (2008).
18) H. Takahashi, H. Hasegawa, and H. Kanai, Jpn. J. Appl. Phys. **53**, 07KF08 (2014).
19) R. Nagaoka, K. Ishikawa, M. Mozumi, M. Cinthio, and H. Hasegawa, Jpn. J. Appl. Phys. **59**, SKKE16 (2020).
20) B. Dunmire, K. W. Beach, K. H. Labs, M. Plett, and D. R. Strandness Jr, Ultrasound Med. Biol. **26**, 1213 (2000).
21) S. Ricci, L. Bass, and P. Tortoli, IEEE Trans. Ultrason. Ferroelectr. Freq. Control **61**, 314 (2014).
22) B. Y. S. Yiu and A. C. H. Yu, IEEE Trans. Ultrason. Ferroelectr. Freq. Control **63**, 1733 (2016).
23) A. S. Podkowa, M. L. Oelze, and J. A. Ketterling, Appl. Sci. **8**, 227 (2018).
24) C. Kasai, K. Namekawa, A. Koyano, and R. Omoto, IEEE Trans. Ultrason. Ferroelectr. Freq. Control **32**, 458 (1985).
25) H. Hasegawa, R. Nagaoka, M. Omura, M. Mozumi, and K. Saito, J. Med. Ultrason. **48**, 13 (2021).
26) H. Hasegawa, R. Nagaoka, M. Omura, M. Mozumi, and K. Saito, J. Med. Ultrason. **48**, 417 (2021).
27) H. Hasegawa, M. Mozumi, M. Omura, R. Nagaoka, and K. Saito, 42th Symp. Ultrason. Electron., 1Pa5–3, 2021.
28) H. Hasegawa and H. Kanai, IEEE Trans. Ultrason. Ferroelectr. Freq. Control **55**, 1921 (2008).
29) J. A. Jensen, S. I. Nikolov, K. L. Gammelmark, and M. H. Pedersen, Ultrasonics **44**, e5 (2006).
30) C. Demené et al., IEEE Trans. Med. Imaging **34**, 2271 (2015).
31) J. Baranger, B. Arnal, F. Perren, O. Baud, M. Tanter, and C. Demené, IEEE Trans. Med. Imaging **37**, 1574 (2018).
32) J. A. Jensen, Med. Biol. Eng. Comput. **34**, 351 (1996).
33) J. A. Jensen and N. B. Svendsen, IEEE Trans. Ultrason. Ferroelectr. Freq. Control **39**, 262 (1992).
34) R. Asami, T. Tanaka, M. Shimizu, Y. Seki, T. Nishiyama, H. Sakashita, and T. Okada, Ultrasound Med. Biol. **45**, 1663 (2019).